# Enhanced fluctuations of interacting particles confined in a box

Jean-Baptiste Delfau, Christophe Coste, Michel Saint-Jean

# Enhanced fluctuations of interacting particles confined in a box

Jean-Baptiste Delfau, Christophe Coste, and Michel Saint Jean
*Laboratoire MSC. UMR CNRS 7057, Université Paris Diderot, and PRES Sorbonne Paris Cité, Bâtiment Condorcet, 10 rue Alice Domon et Léonie Duquet, 75205 Paris Cedex 13, France*
(Received 25 January 2012; published 24 April 2012)

We study the position fluctuations of interacting particles aligned in a finite cell that avoid any crossing in equilibrium with a thermal bath. The focus is put on the influence of the confining force directed along the cell length. We show that the system may be modeled as a 1D chain of particles with identical masses, linked with linear springs of varying spring constants. The confining force may be accounted for by linear springs linked to the walls. When the confining force range is increased toward the inside of the chain, a paradoxical behavior is exhibited. The outermost particles fluctuations are enhanced, whereas those of the inner particles are reduced. A minimum of fluctuations is observed at a distance of the cell extremities that scales linearly with the confining force range. Those features are in very good agreement with the model. Moreover, the simulations exhibit an asymmetry in their fluctuations which is an anharmonic effect. It is characterized by the measurement of the skewness, which is found to be strictly positive for the outer particles when the confining force is short ranged.

DOI: 10.1103/PhysRevE.85.041137 PACS number(s): 05.40.−a, 66.10.cg, 47.57.eb

## I. INTRODUCTION

There has been much recent interest in the behavior of Coulomb clusters. Relevant experiments concern ions in Paul traps [1–4], dusty plasmas [5–7] trapped in electrostatic potential wells, and charged metallic beads in a confinement cell [8]. Ions interact with a long-ranged Coulomb potential, whereas the dust particles are screened by the plasma and interact with a Yukawa potential. Both configurations have been studied in numerical simulations [9–11]. In those studies, the charged particles are confined transversally in such a way that they cannot cross each other and confined longitudinally in a cell of finite length. This geometric ordering implies strong correlations between the particles. Their thermal fluctuations at equilibrium are described by their mean-square displacement (MSD). The time evolution of the MSD have been the focus of several studies [12–15] that have considered hard-core interactions between particles in a line, with reflecting boundary conditions at the extremities. When dealing with finite systems with fixed boundary conditions, one expects the MSD to saturate when all the particles have explored the available space, with a saturation value that depends on the position of the particle in the line. It is shown in Ref. [12] that the shape of the MSD as a function of the particle index is a parabola. This has been confirmed experimentally for chains of cold trapped ions [1,10] or charged beads [8].

In this paper, we consider a finite system of particles that interact with a screened electrostatic potential. They are confined along a line by a transverse harmonic potential and restricted to a cell of finite length by a longitudinal potential. We focus on the influence of the longitudinal confinement force on the thermal fluctuations. The interaction and confinement are chosen in order to be comparable to the experimental values in Ref. [8], but we take advantage of the numerical simulations to extend this study toward parameter ranges that are experimentally out of reach. The dynamics is defined by a system of coupled Langevin equations and studied numerically. We modelize the system as a chain of point masses and springs in a thermal bath. The relevant stiffnesses are uniquely determined once the equilibrium positions of the particles are known from the simulations. We focus on the long-time values of the MSD as a function of the particle index and postpone the study of transitory behaviors to a forthcoming paper [16].

As for hard-core interactions, the constant MSD value reached at long times depends on the position of the particle along the line. For perfectly reflecting walls, that is, for a null confinement range, the particles are equidistant in their equilibrium configuration. The largest fluctuations are observed for the center particle, and they monotonously decrease toward both extremities. When the confinement range increases (for a given cell length), we exhibit an unexpected result: There appears a minimum of the MSD at a finite distance from the walls that scales roughly linearly with the confinement range, as long as this latter is smaller than half the cell length. Moreover, the MSD of the center particle decreases with the confinement range, and the MSD of the outermost particles increases, becoming even larger than that of the center particle when the confinement extends on the whole cell. In this case, the confinement enhances the diffusion. We show that this behavior is peculiar to finite systems and may be interpreted by considering how the shape of the normal modes of vibration of the particles evolves with the confinement range.

This paper is organized as follows: in Sec. II we rapidly describe the molecular dynamic algorithm used in our numerical simulations. We specify the parameters and insist on the averaging process. In Sec. III, we expose our model of a chain of masses and springs in a thermal bath. We classify the different kinds of confining forces according to the stiffness values that they bring about. We also recall how the determination of the eigenmodes of the chain provides all relevant information about particle diffusion. Section IV is devoted to the study of short-ranged confining potentials. The eigenmodes are obtained analytically, using a method developed by Montroll and Potts [17], and then the predictions of the chain model are compared to the simulation data. Section V is concerned with long-ranged confining potentials. In this case, the eigenmodes are calculated numerically once the equilibrium positions of the particles are known. We discuss in Sec. VI an anharmonic effect that is evidenced by

 

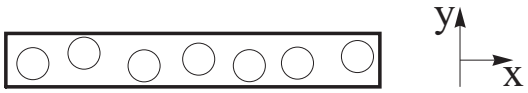


FIG. 1. Scheme of the system.

a nonzero skewness of the MSD histograms. A conclusion (Sec. VII) sum up our results.

## II. NUMERICS

### A. Model and algorithm

The simulations are described at length in Ref. [18]. We shortly summarize them below for the sake of completeness. We consider $(2N-1)$ identical movable-point particles of mass $M$ located in the $xy$ plane, submitted to a thermal bath at temperature $T$. The particles are confined by a quadratic potential in $y$ in such a way that they cannot cross each other, as if they were diffusing in a narrow channel of finite length $L$ (see Fig. 1). A natural length scale is, thus, the mean distance in a homogeneous system, $\overline{d} \equiv L/(2N)$.

Let $\mathbf{r}_n = (x_n, y_n)$ be the position of the particle $n$. The origin is taken as the middle of the cell left side. The particle is submitted to the lateral confinement force $-\beta y_n \mathbf{e}_y$ of stiffness $\beta$ and along the $x$ axis to the longitudinal repulsive confinement forces $F_w(x_n)$ and $F_w(L-x_n)$ from the walls and to the interaction force $\mathbf{F}_{\rm int}(\mathbf{r}_n)$ from the other particles. Each pair of particles $(n,p)$ at respective positions $\mathbf{r}_n$ and $\mathbf{r}_p$ interact with a screened electrostatic interaction described by the force

$$F_0(\mathbf{r}_n - \mathbf{r}_p) = \frac{E_0}{\lambda_0} K_1\left(\frac{|\mathbf{r}_n - \mathbf{r}_p|}{\lambda_0}\right), \tag{1}$$

where $K_1$ is the modified Bessel function of index 1 [19]. The constant $\lambda_0$ is the characteristic decrease length of the interaction and the constant $E_0$ is its energy scale. The interaction force thus reads,

$$\mathbf{F}_{\rm int}(\mathbf{r}_n) = \sum_{p\neq n} \frac{E_0}{\lambda_0} K_1\left(\frac{|\mathbf{r}_n - \mathbf{r}_p|}{\lambda_0}\right) \frac{\mathbf{r}_n - \mathbf{r}_p}{|\mathbf{r}_n - \mathbf{r}_p|}, \tag{2}$$

where the summation extends to all particles in the chain. The longitudinal confinement force is

$$F_w(r) = \frac{E_w}{\lambda_w}\left(\frac{\lambda_w \pi}{2r}\right)^{1/2}\left(1+\frac{\lambda_w}{2r}\right)\exp\left(-\frac{r}{\lambda_w}\right) \tag{3}$$

and is specified by the constant $\lambda_w$, which is the characteristic decrease length of the confinement potential, and by the constant $E_w$, which is its energy scale. This expression is analogous to the electrostatic confining potential in our previous experiments [8]. The divergency of the potential at small $r$ is also numerically suitable. A plot of some examples of those interaction forces is provided in Fig. 2.

We describe the dynamics with the Langevin equation,

$$M\ddot{\mathbf{r}}_n + M\gamma\dot{\mathbf{r}}_n - \mathbf{F}_{\rm int}(\mathbf{r}_n) - [F_w(x_n) - F_w(L-x_n)]\mathbf{e}_x + \beta y_n \mathbf{e}_y = \boldsymbol{\mu}(n,t), \tag{4}$$

with $\gamma$ the damping constant and with $\boldsymbol{\mu}(n,t)$ the random force applied on the particle $n$ at time $t$. The random force has the

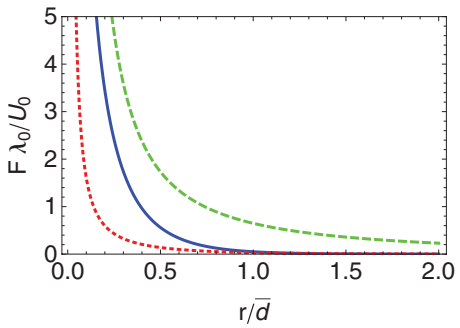


FIG. 2. (Color online) Plot of the dimensionless force $F\lambda_0/E_0$ as a function of the dimensionless distance $r/\overline{d}$. (Solid blue line) Interaction force, $\lambda_0 = \overline{d}/4$. (Dotted red line) Confinement force, $E_w = 0.1E_0$ and $\lambda_w = \overline{d}/2$. (Dashed green line) Confinement force, $E_w = 0.5E_0$ and $\lambda_w = 4\overline{d}$.

statistical properties of a white Gaussian noise,

$$\langle \mu_x(n,t)\rangle = 0, \quad \langle \mu_y(n,t)\rangle = 0, \quad \langle \mu_x(n,t)\mu_y(n',t')\rangle = 0, \tag{5}$$

$$\langle \mu_x(n,t)\mu_x(n't')\rangle = \langle \mu_y(n,t)\mu_y(n',t')\rangle = 2k_B T M\gamma\delta_{n,n'}\delta(t-t'), \tag{6}$$

where $\langle\cdot\rangle$ means statistical averaging, where $k_B$ is Boltzmann's constant and where the Kronecker symbol $\delta_{n,n'}$ is equal to 1 if $n = n'$ and to 0 otherwise. As in Ref. [18], the simulation is based on the Gillespie algorithm [20,21] that allows a consistent time discretization of the Langevin equation. As the initial condition, we put the required number of particles at equidistant places in the cell and let the system evolve. The quantity of interest is the MSD along the $x$ direction,

$$\langle \Delta x^2(n,t)\rangle = \langle [x(n,t+t_0) - x(n,t_0) - \langle x(n,t+t_0) - x(n,t_0)\rangle]^2\rangle, \tag{7}$$

where $t_0$ is an arbitrary initial time and $n$ the index of the particle under study. In the finite length configuration the particles are not equivalent; hence, the ensemble averaging has to be done for a given particle on different simulation runs. The dynamics may be assumed to be stationary, so $\Delta x^2(n,t)$ do not depend on $t_0$. For a given time $t$ and a given particle $n$, it thus makes sense to average on the initial time $t_0$ which greatly improves the statistics. This *double averaging* process is described at length in Ref. [18].

### B. Parameters of the simulation

In what follows, we vary the parameters $(E_w,\lambda_w)$ in order to test the influence of the confining force and keep the other parameters constant. In most simulations, we study a system of 33 particles $(N = 17)$ in a cell of 60 mm, hence, a mean interparticle distance $\overline{d} \equiv L/(2N) = 1.76$ mm. The cell length $L$, the movable particles number $(2N-1)$, the temperature $T$, and the interaction potential are, thus, fixed to values that are close to the experimental ones in our previous study [8]. However, we have also varied the particles number in the range $8 \leqslant N \leqslant 66$ at constant mean density and verified that the system behavior is generic, whatever the value of $N$ [see below Sec. V B and, particularly, Fig. 12(a)].

The length scale of the interaction potential is $\lambda_0 = \overline{d}/4$. The dimensionless parameters $\overline{d}/\lambda_0$ and $E_0/(k_B T) \approx 5$ are chosen to be of the same order of magnitude as in other numerical [9–11] and experimental [5–8] studies. We let the confinement length scale evolve between $\lambda_w = \overline{d}/4$ and $\lambda_w = 15\overline{d}$ (this latter value corresponding to half the cell length) and let the confinement energy evolve between $E_w = E_0/200$ and $E_w = E_0/2$.

The long-time limit of the MSD is independent from the dissipation, as shown by Eq. (20), but the duration of the simulations increases with $\gamma$ because the time step has to be much shorter than $\gamma^{-1}$ and because the asymptotic regime is reached after longer transitory behaviors. We thus choose $\gamma = 1\ \mathrm{s}^{-1}$ for convenience in almost all simulations described in what follows.

### C. Statistical averaging

An important matter is the number of simulation runs required to obtain reproducible results, in particular for higher values of $\gamma$. We have, therefore, undertaken two consistency checks. Since the system is obviously symmetric with respect to the center of the cell, the particles equilibrium positions and their stationary MSD values have to exhibit this symmetry when plotted as functions of the particles index. We have, thus, carefully checked the symmetry of the MSD plots for each parameter set. In order to make the strongest possible test, we have chosen the case of a long-ranged confining force, because this configuration is quite unfavorable as far as the calculation time is concerned.

The long-time MSD is plotted in Fig. 3 for several values of $\gamma$ ranging between $\gamma = 1$ and $\gamma = 20\ \mathrm{s}^{-1}$. A sample without averaging is given as an example, showing a MSD that is indeed not symmetric around the cell center. The result of only averaging four runs for $\gamma = 20\ \mathrm{s}^{-1}$ is also displayed. With this insufficient averaging, some asymmetry is still observed. In contrast, it is clearly seen that the symmetry is recovered after sufficient averaging. The data for $\gamma = 1$ and $\gamma = 5\ \mathrm{s}^{-1}$ have been averaged on 10 samples, and those for $\gamma = 20\ \mathrm{s}^{-1}$ have been averaged on 30 samples. They do not display any significant asymmetry.

The MSD in the saturated regime has to be independent on the dissipation $\gamma$, which controlled the dynamics only.

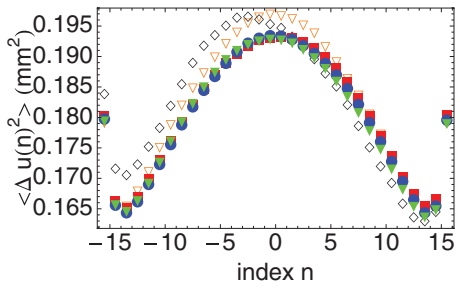


FIG. 3. (Color online) Plot of dimensionless MSD $\langle \Delta u(n)^2 \rangle$ as a function of particle position $n$ for a system of 33 particles, $\lambda_w = 8.25\overline{d}$ and $E_w = 0.1E_0$. (Blue disks) $\gamma = 1\ \mathrm{s}^{-1}$ and 10 averages; (red squares) $\gamma = 5\ \mathrm{s}^{-1}$ and 10 averages; (green triangles) $\gamma = 20\ \mathrm{s}^{-1}$ and 30 averages. Open black diamonds correspond to no averaging; open orange triangles correspond to averaging only four numerical runs.

This constitutes a second consistency check of our simulation data. As shown by Fig. 3, once correctly averaged, the MSD curves for $\gamma = 1$, $\gamma = 5$, and $\gamma = 20\ \mathrm{s}^{-1}$ indeed collapse on the same curve, if one considers the data averaged on four runs only. It is clear that the fluctuations of the outermost particles have reached their stationary regime, in contrast with the inner particles. This comes from the fact that the particle characteristic dynamical times are much greater for the inner particles than for the outermost ones, as will be discussed in a forthcoming paper [16].

This study lead us to reconsider our previous work [8]. Here we have reported on a "camel back" shape for some MSD curves, which is not observed in simulations with proper averaging. The experimental dissipation coefficient was roughly $\gamma = 10\ \mathrm{s}^{-1}$, and we now interpret this shape as a spurious effect due to lack of averaging for the inner particles. We see in Fig. 3 that even when averaging four runs the statistics is insufficient for the particles near the cell center. We may interpret the necessity of a longer averaging to get the long-time behavior of the inner particles from the time evolution of the normal modes that describe the chain dynamics. The dynamics of the inner particles is mostly due to that of the low-frequency modes. Let $\tau_D$ be the characteristic decrease time associated to the component $\omega_s$ of a perturbation. We have $\tau_D \sim Q/\omega_s$, where $Q = \omega_s/\gamma$ is the quality factor. For a total duration $T_{\mathrm{exp}}$, the number of perturbations of frequency $\omega_s$ is $N_{\mathrm{pert}} \sim T_{\mathrm{exp}}/\tau_s$. The noise in the MSD measurements scales as $\sqrt{N_{\mathrm{pert}}} \propto \sqrt{\gamma}/(\omega_s\sqrt{T_{\mathrm{exp}}})$. The noise is, thus, greater for the lower-frequency modes and, thus, for the inner particles.

## III. INTERACTING PARTICLES IN A BOX

### A. A chain of masses and springs

We modelize the system Eq. (4) as a strictly 1D configuration of $(2N+1)$ particles, among which $(2N-1)$ are movable, in an interval of length $L$ of the $x$ axis, at positions $x_n$ with $n \in [-N, N]$. At both ends, two fixed particles such that $x(\pm N, t) = \pm L/2$ for all time $t$ represent the walls. We assume nearest-neighbor interactions between the particles. In order to take into account the confinement force, we assume in the general case that each particle interacts with both walls.

From a given simulation run, the statistically averaged positions of the particles at long times give their equilibrium positions. Since we know all the interactions and confining forces, those equilibrium positions may also be calculated from the Newton equations. The equilibrium position $x_n^*$ of a particle $n$, with $n \in [-N+1, N-1]$, is, thus, given by

$$F_w(x_n^*) - F_w(L - x_n^*) + F_0(x_n^* - x_{n-1}^*) - F_0(x_{n+1}^* - x_n^*) = 0, \tag{8}$$

where the forces $F_0$ and $F_w$ are given in Eqs. (2) and (3).

Let us define the interparticle equilibrium distances $d_n = x_n^* - x_{n-1}^*$. The thermal fluctuations induce small displacements $u_n$ of the particles around their equilibrium positions $x_n^*$, such that $x_n(t) = x_n^* + u_n(t)$ with $|u_n| \ll d_n$. The dynamics of the interacting particles may be described by that of a chain of identical point particles of mass $M$ linked by linear springs to their neighbors. The confinement is accounted for, in the

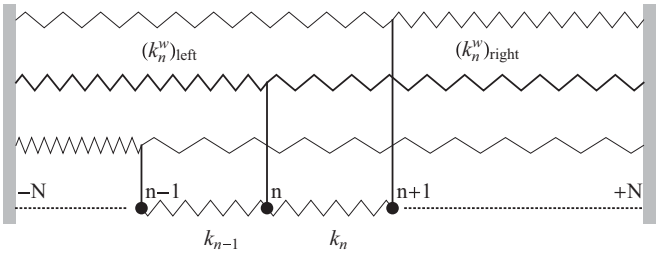


FIG. 4. Schematic description of the chain model. The walls are the gray rectangles. An arbitrary particle of index $n$ and its two neighbors are represented as black dots. They are linked by springs of stiffnesses $k_{n-1}$ and $k_n$, and each particle is linked to the left (right) wall by a spring of stiffness $(k_n^w)_{\text{left}}$ $[(k_n^w)_{\text{right}}]$.

general case, by other linear springs linked between each particle and both walls. The spring stiffnesses are deduced from the forces as

$$k_n \equiv -\frac{\partial F_0}{\partial x}(d_n),$$
$$k_n^w \equiv \left(k_n^w\right)_{\text{left}} + \left(k_n^w\right)_{\text{right}} \equiv -\frac{\partial F_w}{\partial x}(x_n^*) - \frac{\partial F_w}{\partial x}(L - x_n^*), \tag{9}$$

which are, thus, completely determined by the equilibrium positions of the particles $x_n^* = \langle x_n \rangle$. A schematic description of the model is provided in Fig. 4.

When we vary the confinement force parameters $\lambda_w$ and $E_w$, three different configurations may be exhibited. A confining potential is *short-ranged* if each wall interacts with the nearest particle only. Two examples for which the wall influence is limited to the outermost particles are represented in Figs. 5(a) and 5(b), where we plot $d_n$ as a function of the particle index. It is clear that the interparticle distance is a constant $d$, differing from the distance $d_w$ between the outermost particles and the neighboring wall. The chain model is, therefore, greatly simplified, with a constant $k_w$ between the outermost particles and the neighboring wall and a constant $k_n = k$ between all other adjoining particles.

We define $k_w = k(1 - \epsilon)$, where the constant $\epsilon \in [-\infty, 1]$. The value $\epsilon = 0$ corresponds to a uniform chain with $k_w = k$, and separates the *hard wall* configurations ($\epsilon < 0$, $k_w > k$) from the *soft wall* configurations ($\epsilon > 0, k_w < k$). The Fig. 5(a) illustrates the hard wall situation for which $d_w < d$ and $k_w > k$, with $\epsilon = -2.17$, whereas Fig. 5(b) illustrates the soft wall situation for which $d_w > d$ and $k_w < k$, with $\epsilon = +0.42$.

In the third configuration, *long-ranged* confinement, the wall influence extends more toward the interior of the chain, as shown in Figs. 6(a) and 6(b), where we show the interparticle distances $d_n/\overline{d}$ as a function of the particle indices. Such distributions of equilibrium positions are observed for charged ions in Paul traps [1,2,10,11], for confined plasma dusts [7], and for charged metallic beads [8].

In order to describe accurately those latter situations, we must, therefore, assume that the stiffness $k_n$ between particles $n$ and $n+1$ actually depends on their index and introduce for each particle a link with the walls, of stiffness $k_n^w$, that describes the confinement. The index-dependent stiffnesses are displayed in Figs. 6(c) and 6(d), and the stiffnesses between the beads and the left wall are displayed in Figs. 6(e) and 6(f) (those with the right wall are obviously symmetric).

The difference between the columns of Fig. 6 consists in the length scale $\lambda_w$ of the confining force, which is roughly doubled in the right column, whereas the amplitude $E_w$ is kept constant. The distance between the outermost particle and the wall ($d_{\pm 16}/\overline{d} > 1$) increases with the confinement range, which indicates an overall compression of the chain. This is confirmed by the interparticle distance in the middle of the chain, which is 0.88 $\overline{d}$ for Fig. 6(a) and 0.82 $\overline{d}$ for Fig. 6(b). In the same fashion, the interparticles stiffness is more dependent on the index when the confinement range is increased [compare Fig. 6(c) with Fig. 6(d)] and the wall influence extends at larger distances from the walls [compare Fig. 6(e) with Fig. 6(f)].

The equations of motion for the chain are readily obtained from Eq. (4) if we restrict all motions along the $x$ axis and develop to first order in the small quantity $u_n$. We get a set of coupled Langevin equations,

$$M\ddot{u}_n = k_n u_{n-1} - \left(k_n^w + k_n + k_{n+1}\right)u_n + k_{n+1}u_{n+1} - M\gamma\dot{u}_n + \mu(n,t), \tag{10}$$

where $-N \leqslant n \leqslant N$ and with $u(-N,t) = u(N,t) = 0$. This 1D modelization is consistent because of the lateral confinement imposed in our simulations [see Eq. (4)]. We have checked that, in the simulations, all particles are indeed aligned along the cell axis at equilibrium with $\langle y_n \rangle = 0$ when they have reached thermal equilibrium. We have also checked that, for each particle, $\langle \Delta y^2(n,t) \rangle = k_B T/\beta$. This is the MSD for a particle in a harmonic potential of stiffness $\beta$, showing that the longitudinal and transverse motions are decoupled.

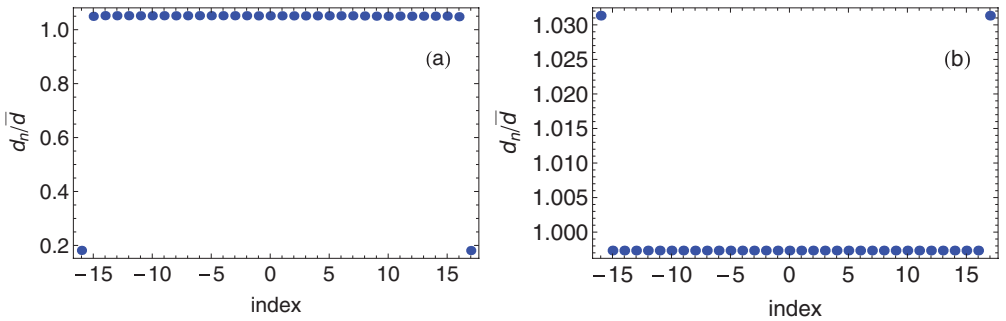


FIG. 5. (Color online) Plot of interparticle distances $d_n/\overline{d}$ as a function of the particle index $n$ for 33 particles ($N = 17$) and short-ranged confinement. (a) Hard wall, $\lambda_w = 0.27\,\overline{d}$, $E_w = 0.0095\,E_0$, $\epsilon = -2.17$. (b) Soft wall, $\lambda_w = 0.57\,\overline{d}$, $E_w = 0.1\,E_0$, $\epsilon = +0.42$.

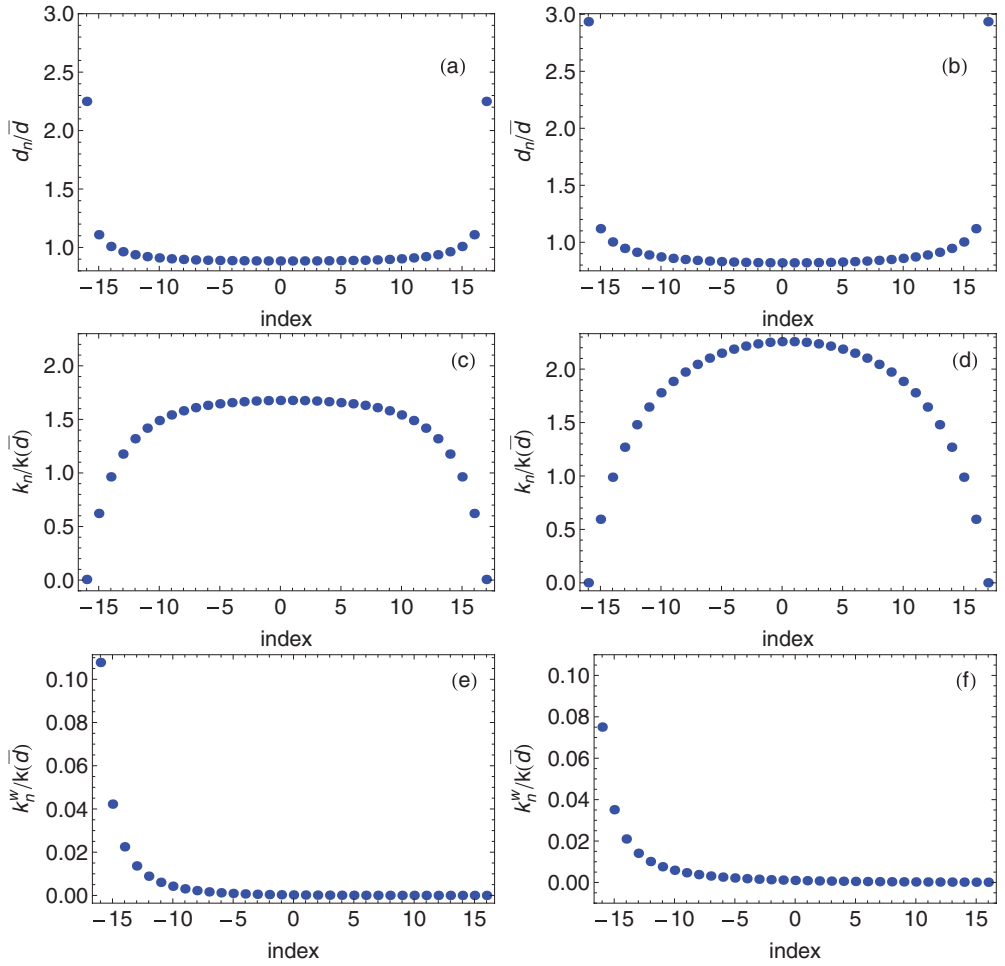


FIG. 6. (Color online) [(a) and (b)] Plot of dimensionless interparticle distances $d_n/\bar{d}$. [(c) and (d)] Plot of dimensionless interparticle stiffnesses $k_n/k(\bar{d})$. [(e) and (f)] Plot of dimensionless stiffnesses between a particle and the left wall $k_n^w/k(\bar{d})$, as a function of the particle index $n$, for $N = 17$. (Left plots) $\lambda_w = 4\,\bar{d}$, $E_w = 0.1\,E_0$. (Right plots) $\lambda_w = 8.5\,\bar{d}$, $E_w = 0.1\,E_0$.

Moreover, the transverse confining stiffness $\beta$ is such that $\langle \Delta y^2(n,t)\rangle \ll \langle \Delta u^2(n,t)\rangle$.

### B. The range of the confining potential

It is convenient to identify the confinement potential length scale $\lambda_w$ and energy scale $E_w$ which result in short-ranged (either hard or soft walls) and long-ranged potentials.

In the short-ranged confinement case, each wall only has an effect on the nearest outermost particle. Hence, all particles in the chain only interact with their nearest neighbors, and the calculation of their equilibirum positions is particularly simple. The distance between neighboring particles is a constant $d$, which automatically ensures consistency with Eq. (8) for $i \in [-N+2, N-2]$. Let $d_w$ be the distance between the outermost particles and the nearby wall. Knowing that $d_w + (N-1)d = L/2$, the only nontrivial equation deduced from Eq. (8) reads,

$$F_w(E_w,\lambda_w,d_w) = F_0[E_0,\lambda_0,d(d_w)]. \tag{11}$$

Let $k_w$ be the stiffness between each outermost particle and the nearby wall and $k$ the stiffness between adjacent particles, so $k_w = k(1-\epsilon)$, where $(\epsilon \leqslant 1)$. We have

$$\frac{\partial F_w}{\partial x}(E_w,\lambda_w,d_w) = (1-\epsilon)\frac{\partial F_0}{\partial x}[E_0,\lambda_0,d(d_w)]. \tag{12}$$

The limit between soft and hard wall configurations takes place at $\epsilon = 0$. Since $F_w \propto E_w$ for a given length scale $\lambda_w$, the relevant values of $d_w$ are the solutions to the equation

$$1 = \frac{\frac{\partial F_w}{\partial x}(E_w,\lambda_w,d_w)F_0[E_0,\lambda_0,d(d_w)]}{\frac{\partial F_0}{\partial x}[E_0,\lambda_0,d(d_w)]F_w(E_w,\lambda_w,d_w)}. \tag{13}$$

The amplitude $E_w$ is then deduced from Eq. (11), thus giving the curve in the plane $(\lambda_w, E_w)$ that separates hard walls from soft walls. This is the dashed red curve in Fig. 7.

Obviously, Eqs. (11) and (12) are valid when the confining potential extends toward the outermost particles only. We define as short-ranged potentials those for which the stiffness between the wall and the next-nearest particle is less than 6% of the stiffness between adjacent particles. In contrast with the criterion used in Eq. (13) which is unambiguous, this coefficient 0.06 is somewhat arbitrary (but small, as it should be). Its value has been chosen for consistency with another criterion which discriminates unambiguously long-ranged confining forces from short-ranged ones, which is

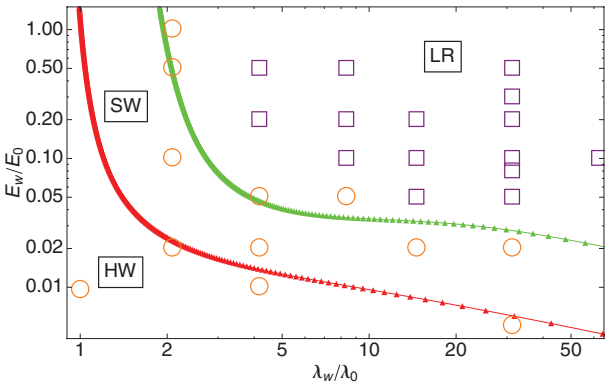


FIG. 7. (Color online) Diagram in the plane $(\lambda_w/\lambda_0, E_w/E_0)$, with both axis in logarithmic scales. The dashed red curve separates hard wall short-ranged potentials (HW) from soft wall ones (SW); see Eq. (13). The solid green curve separates short-ranged potentials from long-ranged potentials (LR); see Eq. (14). (Orange circles) Simulations showing a bell-shaped MSD; see Sec. IV B. (Purple squares) Simulations exhibiting a change of sign for the curvature of the MSD; see Sec. V B.

introduced in Sec. V B and based on the shape of the MSD as a function of the particle indices. For a given $\lambda_w$, the relevant distance $d_w$ is, thus, given by

$$0.06 = \frac{\frac{\partial F_w}{\partial x}[E_w,\lambda_w,d_w + d(d_w)]}{\frac{\partial F_0}{\partial x}[E_0,\lambda_0,d(d_w)]}. \tag{14}$$

Equation (11) then gives the amplitude $E_w$, thus the curve in the plane $(\lambda_w, E_w)$ that separates short-ranged potentials from long-ranged ones. This is the solid green curve in Fig. 7. It is noticeable that a confining force is short ranged either if its characteristic length scale $\lambda_w$ is small whatever its amplitude, which is quite obvious, but also if its amplitude $E_w$ is very small even with a great length scale.

To illustrate this point, let us return to the two examples of short-ranged confinement are displayed in Fig. 5. The distance between particles is indeed a constant $d$, differing from the distance $d_w$ between each outermost particle and the nearby wall. For Fig. 5(a), $\lambda_w \approx \lambda_0$ and $E_w \approx E_0/100$. We may deduce from Eq. (12) the value of the constant $\epsilon$, which is $-2.17$. The relevant point in the plane $(\lambda_w, E_w)$ indeed takes place in the short-ranged hard wall region (HW) of the diagram displayed in Fig. 7. For Fig. 5(b), $\lambda_w \approx 2\lambda_0$ and $E_w \approx E_0/10$. In this case, the value of the constant $\epsilon$ is $+0.42$. The relevant point takes place in the short-ranged soft wall region (SW) of the diagram displayed in Fig. 7, which is consistent with $\epsilon > 0$.

### C. Variance calculations

A complete description of the chain dynamics is obtained when the $(2N-1)$ normal modes of vibrations are identified, as done in Ref. [18]. The characteristic matrix associated to the system of equations (10) is the sparse symmetric matrix,

$$S_{pn} = k_n\delta_{p,n-1} - \left(k_n^w + k_n + k_{n+1}\right)\delta_{n,p} + k_{n+1}\delta_{p,n+1}. \tag{15}$$

The characteristic frequencies $\omega_s$ are given by the eigenvalues $\sigma_s$ of $S_{pn}$, with $\omega_s^2 = \sigma_s/M$. The normal modes $\mathbf{U}_s$ are the eigenvectors of this matrix, with components $U_s(n)$. The displacement $u(n,t)$ of a given particle $n$ at time $t$ is expressed in terms of the normal modes as $u(n,t) = \sum_{s=1}^{2N-1} X_s(t)U_s(n)$. We thus may recast Eq. (10) as

$$\sum_{s=1}^{2N-1} M\ddot{X}_s U_s(n) = \sum_{n'=-N}^{N}\sum_{s=1}^{2N-1} S_{nn'}X_s U_s(n') - M\gamma\sum_{s=1}^{2N-1}\dot{X}_s U_s(n) + \mu(n,t). \tag{16}$$

Taking the scalar product with the mode $\mathbf{U}_{s'}$, using the orthonormality $\mathbf{U}_s \cdot \mathbf{U}_{s'} = \delta_{ss'}$, and the definition of eigenmodes $\sum_{n'=-N}^{N} S_{nn'}U_s(n') = -M\omega_s^2 U_s(n)$, we get

$$\ddot{X}_s + \omega_s^2 X_s + \gamma\dot{X}_s = \frac{\widetilde{\mu}(s,t)}{M}, \tag{17}$$

where we have defined $\widetilde{\mu}(s,t) = \sum_{n=-N}^{N} U_s(n)\mu(n,t)$ and renamed $s$ the dummy index $s'$. It is easy to calculate the correlations of the random force $\widetilde{\mu}(s,t)$ from Eq. (6),

$$\langle\widetilde{\mu}(s,t)\widetilde{\mu}(s',t')\rangle = \sum_{n=-N}^{N}\sum_{n'=-N}^{N} U_s(n)U_s(n')\langle\mu(n,t)\mu(n',t')\rangle = 2k_BTM\gamma\delta_{s,s'}\delta(t-t'), \tag{18}$$

which establishes the obvious physical property that the fluctuations of different modes are uncorrelated.

The MSD of the particle $n$ is

$$\langle\Delta u(n,t)^2\rangle = \sum_{s=1}^{2N-1} U_s(n)^2\left\langle\Delta X_s^2(t)\right\rangle, \tag{19}$$

where we have used the orthogonality of the normal modes. From the equipartition theorem, all modes saturate at long times toward the value $2k_BT/(M\omega_s^2)$. The asymptotic value of the MSD for the particle $n$ is, thus,

$$\lim_{t\to\infty}\langle\Delta u(n,t)^2\rangle \equiv \langle\Delta u(n)^2\rangle = \frac{2k_BT}{M}\sum_{s=1}^{2N-1}\frac{U_s(n)^2}{\omega_s^2}. \tag{20}$$

## IV. SHORT-RANGED CONFINING POTENTIALS

### A. Normal mode calculation

For short-ranged confinement, the normal modes may be determined analytically, using a method of Montroll and Potts [17] for a chain with mass impurities. We treat the case of impurities characterized by different stiffnesses. Let us assume that the spring between the two particles $-m-1$ and $-m$ (respectively, $m$ and $m+1$) is of stiffness $k'$, with all others stiffnesses being equal to $k$. The normal modes of Eq. (10) may be searched as $u_n(t) = U(n)e^{i\omega t}$, where $i^2 = -1$ and

$$U(n) = \begin{cases} A\sin(N+n)\phi & \text{if} \quad n > m \\ B\sin(N-n)\phi & \text{if} \quad n < -m, \\ Ce^{in\phi} + De^{-in\phi} & \text{otherwise.} \end{cases} \tag{21}$$

The equations for all particles except those at $\pm m$ and those at $\pm(m+1)$ are satisfied if

$$M\omega^2 = 2k(1-\cos\phi), \tag{22}$$

which gives the frequency $\omega$ as a function of the parameter $\phi$. The constants $A$, $B$, $C$, and $D$ are determined by the equations of motions for particles $-m-1, -m, m$, and $m+1$. Introducing $k' = k(1-\epsilon)$, a little algebra gives

$$\begin{aligned}
&(A+B)[\epsilon \sin(N-m-1)\phi - \sin(N-m)\phi] \\
&\quad = -2(1-\epsilon)(C+D)\cos m\phi, \\
&(A+B)(1-\epsilon)\sin(N-m-1)\phi \\
&\quad = -2(C+D)[\epsilon \cos m\phi - \cos(m+1)\phi], \\
&(A-B)[\epsilon \sin(N-m-1)\phi - \sin(N-m)\phi] \\
&\quad = -2i(1-\epsilon)(C-D)\sin m\phi, \\
&(A-B)(1-\epsilon)\sin(N-m-1)\phi \\
&\quad = -2i(C-D)[\epsilon \sin m\phi - \sin(m+1)\phi],
\end{aligned} \tag{23}$$

leading us to distinguish even modes ($A = B, C = D$) from odd ones ($A = -B, C = -D$).

In our case, the peculiar links are between the outermost particles and the walls, so $m = \pm(N-1)$ and $k' = k_w$. The characteristic frequencies are given by

$$\begin{aligned}
\epsilon \cos(N-1)\phi_s &= \cos N\phi_s, \quad \text{(even modes)}, \\
\epsilon \sin(N-1)\phi'_s &= \sin N\phi'_s, \quad \text{(odd modes)}.
\end{aligned} \tag{24}$$

With soft walls (that is, $\epsilon > 0, k_w < k$), there are $N$ even modes and $N-1$ odd modes with real parameters $\phi_s$ and $\phi'_s$. The roots are located between adjacent zeros of, respectively, $\cos(N\phi_s)$ and $\sin(N\phi_s)$ and, thus, very easy to find numerically.

With hard walls we have $\epsilon < 0$ and $k_w > k$. When $\epsilon < -1$, the highest-frequency modes are no longer given by Eq. (24). They are recovered assuming a complex $\phi = \pi + i\psi$, which gives

$$\begin{aligned}
&|\epsilon| \cosh(N-1)\psi_N = \cosh N\psi_N, \quad \text{(when } \epsilon < -1\text{)}, \\
&|\epsilon| \sinh(N-1)\psi'_{N-1} = \sinh N\psi'_{N-1}, \\
&\text{[when } \epsilon < -N/(N-1)\text{]}.
\end{aligned} \tag{25}$$

The frequency is then such that $M\omega^2 = 2k(1+\cosh\psi)$. It is not surprising to get higher frequencies than in the case of soft walls and real $\phi$ as in Eq. (22), since two springs have been replaced by springs of higher stiffnesses. The appearance of a complex parameter with imaginary part $\psi$, hence, of a nonpropagative mode with oscillations located at the extremities of the chain, is reminiscent of the localized mode that appears in a semi-infinite chain when the spring at the free extremity is replaced by one of higher stiffness [22].

With the frequencies given by Eqs. (24) or (25), the normal modes are known and read

$$\begin{aligned}
U_s(n) &= C_s \cos n\phi_s, \\
C_s^2 \sum_{n=-N+1}^{N-1} \cos^2 n\phi_s &= 1, \quad \text{(even modes)}, \\
U_s(n) &= C_s \sin n\phi'_s, \\
C_s^2 \sum_{n=-N+1}^{N-1} \sin^2 n\phi'_s &= 1, \quad \text{(odd modes)},
\end{aligned} \tag{26}$$

where the circular trigonometric functions are replaced by their hyperbolic analogs when complex values of $\phi$ have to be considered. For the sake of comparison and further reference, we recall that, for a homogeneous chain ($k_w = k$ or $\epsilon = 0$), the normal modes are given by

$$\omega_p^2 = 4\frac{k}{M}\sin^2\frac{p\pi}{4N}, \quad U_p(n) = \begin{cases} (1/\sqrt{N})\sin[p\pi n/(2N)], & \text{(odd modes, } p \text{ even)}, \\ (1/\sqrt{N})\cos[p\pi n/(2N)], & \text{(even modes, } p \text{ odd)}, \end{cases} \tag{27}$$

Several modes for short-ranged potentials (26) are displayed in Fig. 8 for soft and hard walls. The low-frequency modes are very similar and do not differ much from the modes of a homogeneous chain [see Figs. 10(a) and 10(b)]. On the contrary, the high-frequency modes in the hard wall case are nothing like those for the soft wall. As seen in Figs. 8(c) and 8(d), the motion of the inner particles is almost completely suppressed. The physical interpretation is clear: The highest frequencies in the hard wall case ($k_w > k$) are greater than the cutoff frequency of the homogeneous chain with stiffness $k$, so the motion does not propagate from the outer particles toward the inner ones. The highest-frequency modes are, hence, localized close to the chain extremities [22].

### B. Saturation values of the MSD

The normal modes (26) allow the calculation of the MSD of each particle at long time (20). A comparison of simulation data for hard walls and soft walls is shown in Fig. 9. The calculations of the MSD are in very good agreement with the data. The MSD of the outer particles is smaller for hard walls, which is consistent with the shape of the normal modes displayed in Fig. 8. In Eq. (20), the mode's amplitude is weighted by the squared normal frequency, which enhances the importance of the low-frequency modes. For the low-frequency modes, the motion of the inner (outer) particles is indeed greater (smaller) in the hard (soft) wall configuration. This is consistent with the fact that the outermost particles are linked to the wall by a harder spring than the inner ones. The MSD of the inner particles is larger, because the interparticle distance is larger for the hard wall configuration, as shown by the comparison of Figs. 5(a) with 5(b).

This shape of the MSD distribution, maximum for the center bead and minimum for the outermost beads, is characteristic of short-ranged potentials. It is observed for all circles placed on the graph in Fig. 7, which are all short-ranged in the sense of the definition given in Sec. III B, see Eq. (14). The same shape is also observed in finite systems of hard-core interacting particles with reflecting boundaries [12]. It was shown in Ref. [8] that, for our experimental conditions, which are roughly

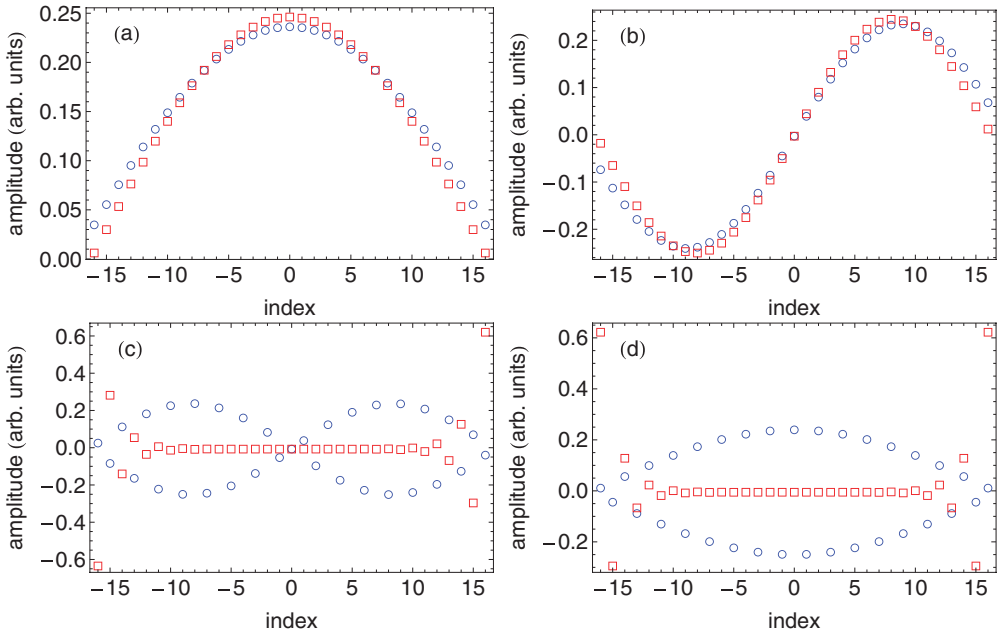


FIG. 8. (Color online) Plot of the normalized amplitude of the normal modes of a chain of 33 particles as a function of the particle's index for short-ranged confinement. Blue circles denote a soft wall configuration $\epsilon = 0.42$ and red squares denote a hard wall configuration $\epsilon = -2.17$. (a) Mode $s = 1$. (b) Mode $s = 2$. (c) Mode $s = 32$. (d) Mode $s = 33$. The modes are ordered by increasing frequency.

the same as in our simulations, the shape of this curve is a parabola.

## V. LONG-RANGED CONFINING POTENTIALS

### A. Normal modes calculation

In that case, we cannot get an analytic expression for the normal modes, but we may numerically obtain the eigenvalues and eigenvectors of the matrix $S_{pn}$ that sum up all information on the system [see Eq. (15)]. Some modes are plotted in Fig. 10. They differ considerably from those for short-ranged potentials (see Fig. 8). Because of the confinement, the high-frequency modes are almost suppressed for the outer beads, whereas the low-frequency modes are emphasized. This has strong consequences on the long-time MSD, because we see in Eq. (19) that the normal mode amplitude is divided by the squared frequency $\omega_s^2$, hence, that the low-frequency contributions are dominant.

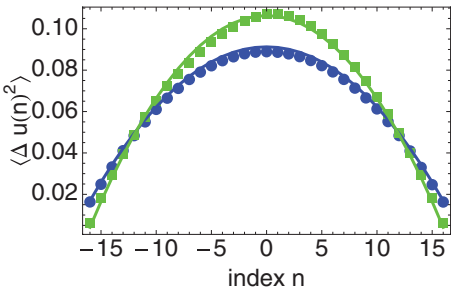


FIG. 9. (Color online) Plot of dimensionless MSD $\langle \Delta u(n)^2 \rangle / \overline{d}^2$ as a function of index $n$, for 33 particles and short-ranged confinement. Simulations are accounted for by discrete symbols, calculations by solid lines of the same color. (Blue disks) Hard wall, $\lambda_w = 0.27\,\overline{d}$, $E_w = 0.0095\,E_0$ [see Fig. 5(a)]. (Green solid squares) Soft wall, $\lambda_w = 0.57\,\overline{d}$, $E_w = 0.1\,E_0$ [see Fig. 5(b)].

### B. Saturation values of the MSD

In order to discuss the long-ranged confinement force, we plot the long-time values of the MSD in Figs. 11(a) and 11(b) for an interaction strength $E_w = 0.1\,E_0$ and a confinement range $\lambda_w$ increasing from $0.57\,\overline{d}$ up to $17.0\,\overline{d}$ and in Fig. 11(c) for a confinement range $\lambda_w = 8.50\,\overline{d}$ and an interaction strength increasing from $E_w = 0.005\,E_0$ up to $E_w = 0.5\,E_0$. The configurations $(\lambda_w = 0.57\,\overline{d}, E_w = 0.1\,E_0)$ and $(\lambda_w = 8.50\,\overline{d}, E_w = 0.005\,E_0)$ both correspond to short-ranged potentials, and the respective MSD plots have the same shape as inw Fig. 9. The other configurations belongs to the long-ranged potentials domain in plane $(\lambda_w, E_w)$.

In those cases, we see that the shape of the MSD plot as a function of the particle index differs from what it was for short-ranged potentials, progressively losing its bell-shaped appearance the further the relevant point in plane $(\lambda_w, E_w)$ moves away the solid green line toward the LR area. The MSD as a function of the particle index ceases to be convex, in contrast with the case of short-ranged potentials, as shown by Fig. 9. This justifies *a posteriori* the numerical value used in Eq. (14) since points $(\lambda_w, E_w)$ corresponding to a nonconvex MSD distribution take place above the curve defined by Eq. (14). It is noteworthy that this perfect agreement between both criteria allows us to determine the confinement range directly from the MSD distribution measurements.

When the confinement parameters take place in the LR area of the diagram Fig. 7, a somewhat paradoxical effect takes place. The fluctuations of the outermost particles are strongly enhanced, while those of the inner particles are

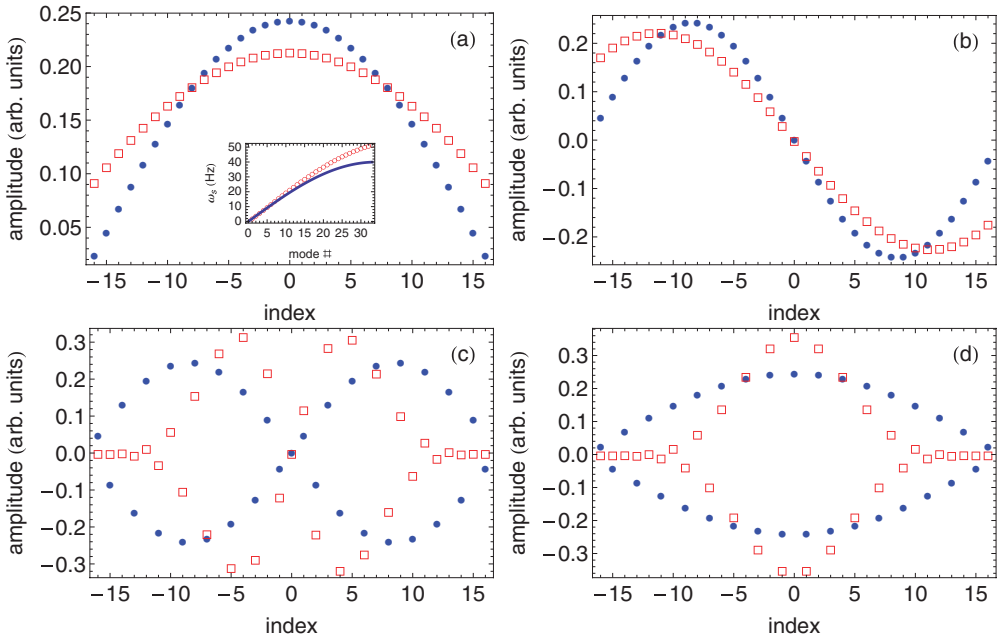


FIG. 10. (Color online) Normalized amplitude of the normal modes for 33 particles as a function of the particle's index. The blue solid disks show for reference the modes of a homogeneous chain Eq. (27) and the open red squares the modes for a confinement range $\lambda_w = 3.96\,\overline{d}$ and $E_w = 0.1E_0$. (a) Mode $s = 1$. In the inset we plot the frequency spectrum $\omega_s$ (Hz) as a function of the mode index $s$ for a chain of 33 particles. (Solid line) Homogeneous chain; (red circles) confinement range $\lambda_w = 3.96\,\overline{d}$ and $E_w = 0.1E_0$. (b) Mode $s = 2$. (c) Mode $s = 32$. (d) Mode $s = 33$. The modes are ordered by increasing frequencies.

reduced, until they become lower than the fluctuations of the outermost particles for the longest-range confining force, with $(\lambda_w = 31.28\,\lambda_0, E_w = 0.5\,E_0)$ [see the orange triangles in Fig. 11(c)]. This enhancement of the fluctuations may reach a factor 4 and do not increase much when $\lambda_w$ is greater than $14.57\,\lambda_0$ for $E_w = 0.1E_0$ [see Fig. 11(b)]. Not only is this

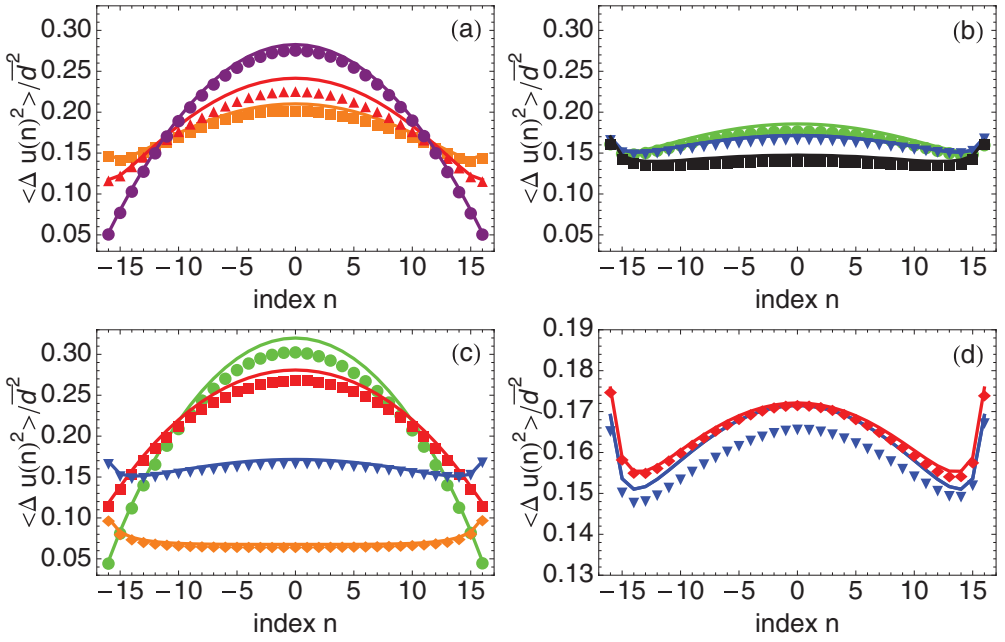


FIG. 11. (Color online) Plot of dimensionless MSD $\langle \Delta u(n)^2 \rangle / \overline{d}^2$ as a function of particle position $n$ for 33 particles and $\gamma = 1\ \mathrm{s}^{-1}$. Discrete symbols simulations data, averaged 10 times; solid lines, with the same color code, calculations from Eq. (19). (a) $E_w = 0.1E_0$; (violet disk) $\lambda_w = 2.10\,\lambda_0$, (red triangles) $\lambda_w = 8.35\,\lambda_0$, and (orange squares) $\lambda_w = 14.57\,\lambda_0$. (b) $E_w = 0.1E_0$; (green disks) $\lambda_w = 22.93\,\lambda_0$, (blue triangles) $\lambda_w = 31.28\,\lambda_0$, and (black squares) $\lambda_w = 62.56\,\lambda_0$. (c) $\lambda_w = 31.28\,\lambda_0$; (green disks) $E_w = 0.005\,E_0$, (red squares) $E_w = 0.02\,E_0$, (blue triangles) $E_w = 0.1\,E_0$ and (orange diamonds) $E_w = 0.5\,E_0$. (d) $E_w = 0.1E_0$, $\lambda_w = 31.28\,\lambda_0$. (Blue triangles) Same curve as in (b). (Red diamonds) Simulations restricted to nearest-neighbors interactions.

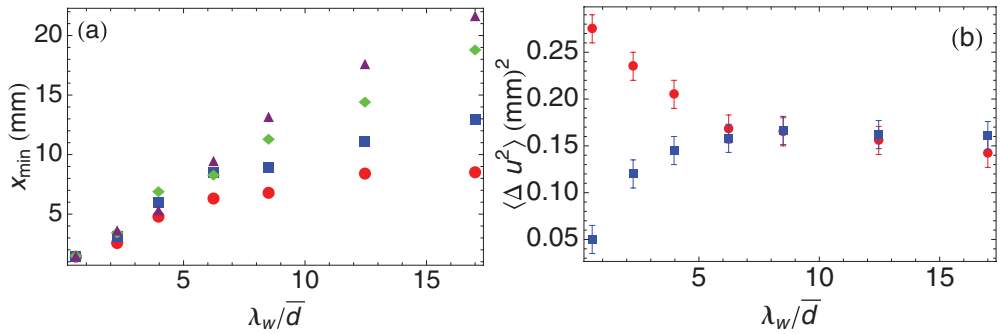


FIG. 12. (Color online) (a) Plot of $x_{\min}$ (in mm) as a function of the (dimensionless) potential range $\lambda_w/\overline{d}$ for a fixed value $\overline{d} = 60/34$ mm and a fixed potential amplitude $E_w = 0.1E_0$. The particles number are, respectively, 16 (green diamonds), 33 (red disks), 66 (blue squares), and 132 (purple triangles). (b) Value of the MSD (in mm$^2$) for the central particle (red disks) and the outer particles (blue squares) as a function of $\lambda_w/\overline{d}$ for a system of 33 particles.

effect strong, but it is also very sensitive to the confining force range. Indeed, a typical lengthscale $\lambda_w \approx 4\overline{d}$ is sufficient to reach the highest values of the outermost particles fluctuations. The inner particles fluctuations are reduced by, at most, a factor 2 for the largest $\lambda_w$, so the reduction of fluctuations for the inner particles is much more gradual than the enhancement of the fluctuations for the outer particles.

As was already noted, the shape of the MSD as a function of the particles index is very different for long-ranged confinement than for short-ranged ones. As soon as the parameters $(\lambda_w, E_w)$ take place in the LR area of Fig. 7, the fluctuations for the immediate neighbors of the outermost beads are minimal. When $\lambda_w$ increases, the distance $x_{\min}$ between the confining walls and the particles exhibiting those minima increases, the MSD of the outermost particle increases, and the MSD of the center particle decreases. Those results are summarized in Fig. 12.

In Fig. 12(a) we plot $x_{\min}$ as a function of $\lambda_w$ at constant $E_w$. For 33 particles, the position of the minimum scales linearly at small $\lambda_w$ and then seems to saturate. This saturation is a finite-size effect. In order to verify this interpretation, we have varied the particle number, keeping the mean interparticle distance $\overline{d}$ constant. In every case a minimum of the MSD appear at a distance $x_{\min}$ from each wall, and this distance scales linearly with $\lambda_w$ at small $\lambda_w$. For the smaller system (16 particles) the saturation is very clear, while for the larger system (132 particles) the linear evolution is effective up to $\lambda_w = 17\overline{d}$. The saturation value is about half the cell length.

The data displayed in Fig. 12(b) show that the MSD for the center (outermost) particle decreases (increases) with the confinement range. Eventually, the MSD for the outermost particle is greater than for the center one. The same behavior is always observed, whatever the particle number, at fixed $\overline{d}$.

A look at the structure of the normal modes, as in Fig. 10, may explain this behavior. The lowest-frequency modes [see Figs. 10(a) and 10(b)] roughly keep their shape, but the motion of the outermost particle is enhanced while that of the center particle is reduced. This is due to the fact that the link between the outermost particle and the fixed wall is of low stiffness, whereas most of the other particles are linked with higher-stiffness springs, as shown by Figs. 6(c) and 6(d). The contribution of the low-frequency modes to the sum in Eq. (20) increases the relative contribution of the outermost particle. Considering now the highest-frequency modes [see Figs. 10(c) and 10(d)], we see that the motion of the particles near both extremities is almost completely suppressed, with a typical length scale equal to $\lambda_w$. This is of no consequence for the outermost particle, because its dynamics is completely dominated by the low-frequency modes. In contrast, the suppression of the high-frequency motion significantly reduces the size of the fluctuations of the other outer particles. This justifies the appearance of a minimum of MSD at a finite distance from the extremities and indicates that the position of this minimum should scale as $\lambda_w$, as shown in Fig. 12(a). Moreover, increasing the confinement range $\lambda_w$ reduces the amplitude of the center particle MSD and increases that of the outer particles at low frequency. Since the contributions to the sum in Eq. (20) are weighted by the factor $1/\omega_s^2$, this explains why the fluctuations decrease for the center particle and increase for the outermost particle when $\lambda_w$ rises, as shown in Fig. 12(b).

In Figs. 11(a)–11(c), we plot the theoretical prediction for the MSD, deduced from Eq. (20) and the calculation of the normal modes based on the equilibrium positions of the particles and on the assumption of nearest-neighbor interactions. The agreement between simulations and calculations is excellent. Some discrepancies appear for the inner particles only, for the longest-ranged confining force, as evidenced by the data displayed as blue triangles in Fig. 11(d) [they are the same as in Fig. 11(b) with a different scale]. When the particles are most strongly confined, the distances between the inner particles is so short that the assumption of interactions restricted to nearest neighbors ceases to be correct. Indeed, when we undertake a simulation restricted to nearest-neighbors interactions, as shown by the red diamonds in Fig. 11(d), the agreement between the simulations and the model is almost perfect. This reveals some limitations of the chain model but constitutes a minor quantitative effect, and taking into account interactions extended to more than the nearest neighbors should be an undue complication.

## VI. ANHARMONIC EFFECTS

In a chain of particles harmonically bounded to their neighbors and the confining walls, the fluctuations around the

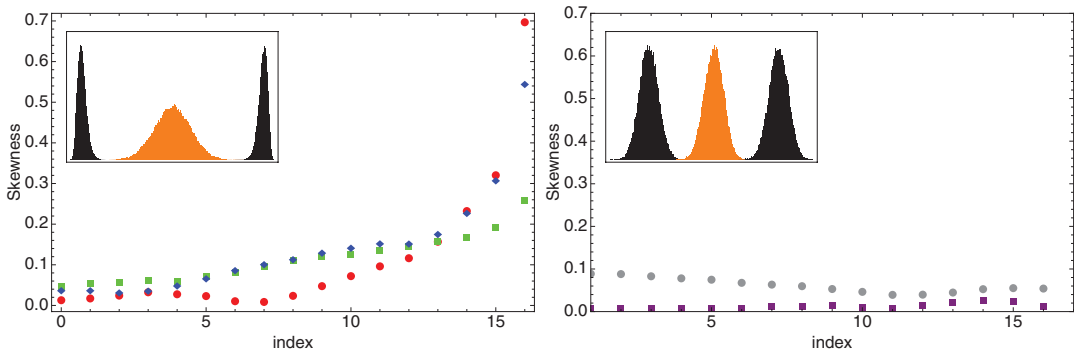


FIG. 13. (Color online) Plot of the skewness as a function of index $n$, for 33 particles, in a half cell. The center particle has index 0. (Inserts) The position histograms (translated for convenience) for the outermost particles and the center one. Left plot, short-ranged confinements: red disks $\lambda_w = \lambda_0$, $E_w = 0.095E_0$, (green squares) $\lambda_w = 2\lambda_0$, $E_w = 0.1E_0$, (blue diamonds) $\lambda_w = 15\lambda_0$, $E_w = 0.005E_0$. Right plot, long-ranged confinements: confinement amplitude $E_w = 0.1E_0$. (Gray disks) $\lambda_w = 15\lambda_0$; (purple squares) $\lambda_w = 30\lambda_0$.

equilibrium have to be symmetrical since each particle is in the bottom of a parabolic well. This is also obvious for the normal modes, which behave like damped harmonic oscillators [see Eq. (17)]. However, asymmetrical fluctuation histograms were observed experimentally for the outermost particles [8]. This is, thus, an anharmonic effect, showing that the linear springs chain cannot explain this feature of the confined particles dynamics. An efficient way to measure the asymmetry of a statistical distribution is to calculate the skewness, which is defined as $\langle (x - \langle x \rangle)^3 \rangle / \langle \Delta x^2 \rangle^{3/2}$ (see, e.g., Ref. [23]).

The skewness measurements are plotted in Fig. 13 as a function of the particle indices. In the left plot, we display data for a short-ranged confining force. The simulations data are in agreement with the experimental observations. The skewness is indeed nonzero, decreasing with the distance from the wall for a given confining force. We see also that the shorter the range of the confining force, the greater the skewness. For the outermost particles, the asymmetry is sufficiently high to be observed right away on the position histograms. Because of obvious symmetry argument, the skewness should be zero for the center particle. The nonzero value measured for this particle gives an indication of the error bars of such measurements.

We display in the right plot of Fig. 13 the skewness for a long-ranged confining force. The skewness remains very small whatever the particle under consideration. In fact, the amplitude of the skewness for the center particle ($n = 0$) is under the error bar and is null by symmetry. The histograms plotted in the inset of the right plot in Fig. 13 are the same for every particle. When the confining force range is increased, the asymmetry of the position histograms observed in the short-ranged case disappears.

Such an effect has been predicted by Lizana and Ambjörnsson [14] for hard spheres confined by perfectly reflecting walls. In this model, the confining force is of stricly null range and the asymmetry of the histograms for the outer particles is strongly emphasized. It is, thus, consistent to observe such an asymmetry in our system with non-zero-ranged forces for the shorter-ranged confining forces. An asymmetry of the fluctuation histograms for the outermost particles has also been reported previously in our experiments [8]. We have checked that the parameters of the confining force in our experiments are close to the short-ranged area defined in Fig. 7, which is consistent with the behaviors observed in the simulations.

## VII. CONCLUSION

In this paper we studied the position fluctuations (the MSD) of interacting particles aligned in a finite cell, when they are in equilibrium with a thermal bath. We focus on the influence of the longitudinal confining force, keeping constant all other parameters in the simulation (e.g., particle number, temperature, and interaction potential).

We modelize the system as a chain of particles strictly aligned along a line, with identical masses, linked with linear springs of varying spring constants. We added to each particle two linear springs bound to each cell extremity to take into account the confining forces. We show that once the normal modes of vibrations are known for the chain, the thermal fluctuations are fully determined. We distinguish between long-ranged confinement that extends at least to the second particle near the wall and short-ranged confinement which is restricted to the outermost particles only. In this latter case the normal modes are calculated analytically, whereas we must resort to numerics for long-ranged confinement.

For short-ranged confinement, the variation of the MSD with the particle index $n$ ($n = 0$ in the center) is bell shaped, with the inner particles exhibiting the highest fluctuations. When the confining force influence is extended toward the inside of the chain, we exhibit a paradoxical behavior. The outermost particles fluctuations are enhanced, whereas those of the inner particles are reduced. They eventually become smaller than the outer-particle fluctuations when the confining force extends toward the middle of the cell. Two minima of fluctuations are observed near the chain extremities, symmetric with respect to the center particle. The gap between the cell extremities and those minima scales as the confining force range. The observed values of the MSD in the simulations are in good agreement with the calculations based on the equilibrium positions of the particles.

The MSD of the outer particles is not symmetrical for the short-ranged confining force. This is an anharmonic effect that cannot be described by our harmonic chain model. We have measured the skewness and showed that it is positive for the outer particles, beyond the measurement uncertainties. It decreases from the outermost particles toward the inner ones and decreases with the range of the confining force. We recover, although in a less pronounced fashion, an effect already seen for particles with hard-core interactions [14].

In a forthcoming paper [16], we will show that our analysis in terms of normal modes determines also the complete dynamics of the system. Moreover, the distinction between short-ranged and long-ranged potentials is also relevant to characterize the different dynamical regimes.


[1] M. G. Raizen, J. M. Gilligan, J. C. Bergquist, W. M. Itano, and D. J. Wineland, Phys. Rev. A **45**, 6493 (1992).

[2] I. Waki, S. Kassner, G. Birkl, and H. Walther, Phys. Rev. Lett. **68**, 2007 (1992).

[3] S. Seidelin, J. Chiaverini, R. Reichle, J. J. Bollinger, D. Leibfried, J. Britton, J. H. Wesenberg, R. B. Blakestad, R. J. Epstein, D. B. Hume, W. M. Itano, J. D. Jost, C. Langer, R. Ozeri, N. Shiga, and D. J. Wineland, Phys. Rev. Lett. **96**, 253003 (2006).

[4] R. Blatt and D. Wineland, Nature **453**, 1008 (2008).

[5] B. Liu and J. Goree, Phys. Rev. E **71**, 046410 (2005).

[6] A. Melzer, Phys. Rev. E **73**, 056404 (2006).

[7] T. E. Sheridan and K. D. Wells, Phys. Rev. E **81**, 016404 (2010).

[8] J.-B. Delfau, C. Coste, C. Even, and M. Saint Jean, Phys. Rev. E **82**, 031201 (2010).

[9] J. P. Schiffer, Phys. Rev. Lett. **70**, 818 (1993).

[10] D. H. E. Dubin, Phys. Rev. E **55**, 4017 (1997).

[11] J. P. Schiffer, J. Phys. B. **36**, 511 (2003).

[12] H. van Beijeren, K. W. Kehr, and R. Kutner, Phys. Rev. B **28**, 5711 (1983).

[13] C. Rödenbeck, J. Kärger, and K. Hahn, Phys. Rev. E **57**, 4382 (1998).

[14] L. Lizana and T. Ambjörnsson, Phys. Rev. Lett. **100**, 200601 (2008).

[15] L. Lizana and T. Ambjörnsson, Phys. Rev. E **80**, 051103 (2009).

[16] J.-B. Delfau, C. Coste, and M. Saint Jean, submitted to Phys. Rev. E (2012).

[17] E. Montroll and R. Potts, Phys. Rev. **100**, 525 (1955).

[18] J.-B. Delfau, C. Coste, and M. Saint Jean, Phys. Rev. E **84**, 011101 (2011).

[19] I. Gradshteyn and I. Ryzhik, *Table of Integrals, Series, and Products* (Academic Press, San Diego, 2007).

[20] D. T. Gillespie, Phys. Rev. E **54**, 2084 (1996).

[21] D. T. Gillespie, Am. J. Phys. **64**, 225 (1996).

[22] M.-C. Desjonqueres and D. Spanjaard, *Concepts in Surface Physics* (Springer, Berlin, 1996).

[23] D. Lemons, *An Introduction to Stochastic Processes in Physics* (John Hopkins University Press, Baltimore, 2002).